JACS
JOURNAL OF THE AMERICAN CHEMICAL SOCIETY
Article
pubs.acs.org/JACS

Critical Role of Alkyl Chain Branching of Organic Semiconductors in Enabling Solution-Processed N-Channel Organic Thin-Film Transistors with Mobility of up to 3.50 $cm^2 V^{-1} s^{-1}$

Fengjiao Zhang,[†,▽] Yunbin Hu,[‡,▽] Torben Schuettfort,[§] Chong-an Di,*[,†] Xike Gao,*[,‡] Christopher R. McNeill,*[,∥] Lars Thomsen,[⊥] Stefan C. B. Mannsfeld,[#] Wei Yuan,[‡] Henning Sirringhaus,[§] and Daoben Zhu*[,†]

[†]Beijing National Laboratory for Molecular Sciences, Key Laboratory of Organic Solids, Institute of Chemistry, Chinese Academy of Sciences (CAS), Beijing 100190, China

[‡]Laboratory of Materials Science, Shanghai Institute of Organic Chemistry, CAS, 345 Lingling Road, Shanghai 200032, China

[§]Cavendish Laboratory, University of Cambridge, JJ Thomson Avenue, Cambridge CB3 0HE, United Kingdom

[∥]Department of Materials Engineering, Monash University, Clayton, Victoria 3800, Australia

[⊥]The Australian Synchrotron, 800 Blackburn Road, Clayton, Victoria 3168, Australia

[#]Stanford Synchrotron Radiation Lightsource, SLAC National Accelerator Laboratory, Menlo Park, California, 94025, United States

Supporting Information

ABSTRACT: Substituted side chains are fundamental units in solution processable organic semiconductors in order to achieve a balance of close intermolecular stacking, high crystallinity, and good compatibility with different wet techniques. Based on four air-stable solution-processed naphthalene diimides fused with 2-(1,3-dithiol-2-ylidene)malononitrile groups (NDI-DTYM2) that bear branched alkyl chains with varied side-chain length and different branching position, we have carried out systematic studies on the relationship between film microstructure and charge transport in their organic thin-film transistors (OTFTs). In particular synchrotron measurements (grazing incidence X-ray diffraction and near-edge X-ray absorption fine structure) are combined with device optimization studies to probe the interplay between molecular structure, molecular packing, and OTFT mobility. It is found that the side-chain length has a moderate influence on thin-film microstructure but leads to only limited changes in OTFT performance. In contrast, the position of branching point results in subtle, yet critical changes in molecular packing and leads to dramatic differences in electron mobility ranging from ~0.001 to >3.0 $cm^2 V^{-1} s^{-1}$. Incorporating a NDI-DTYM2 core with three-branched *N*-alkyl substituents of $C_{11,6}$ results in a dense in-plane molecular packing with an unit cell area of 127 $Å^2$, larger domain sizes of up to 1000 × 3000 nm^2, and an electron mobility of up to 3.50 $cm^2 V^{-1} s^{-1}$, which is an unprecedented value for ambient stable n-channel solution-processed OTFTs reported to date. These results demonstrate that variation of the alkyl chain branching point is a powerful strategy for tuning of molecular packing to enable high charge transport mobilities.

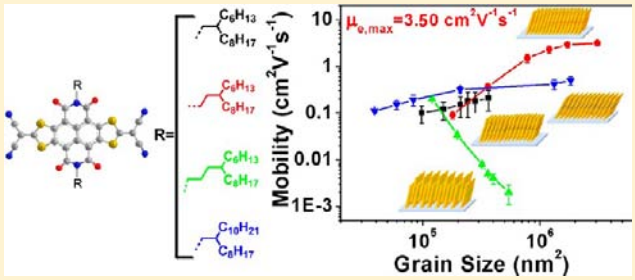

1. INTRODUCTION

Building on rapid developments and tremendous progresses in the past two decades, organic thin-film transistors (OTFTs) have been successfully demonstrated in various applications, such as chemical/biosensors, electronic paper, and radio frequency identification cards (RFIDs).[1−12] In spite of these great achievements, getting the true benefits of OTFTs in ultralow-cost applications still remains a challenging task. Fabrication of high-performance OTFTs via solution processing techniques including roll-to-roll, spin coating, and inkjet printing, etc. is widely believed to be a promising way to solve this problem.[13−23] Very recent results indicate that high mobilities well over 3.0 $cm^2 V^{-1} s^{-1}$ can be achieved by many p-channel OTFTs based on solution processed small molecular and polymeric semiconductors.[20,24−29] These mobility values are comparable with the performance of vacuum deposited OTFTs and approach the mobility of many organic single-crystal transistors. To match the exciting progresses of solution-processed p-channel devices, high-performance n-channel OTFTs are highly desired since only few solution-processed n-channel OTFTs exhibit mobilities >0.50 $cm^2 V^{-1} s^{-1}$.[30−37] This uneven development makes the exploration of solution processable, air-stable n-type semiconductors and the construction of high-performance solution-processed n-channel devices a key issue in organic electronics.

Received: November 26, 2012
Published: January 18, 2013

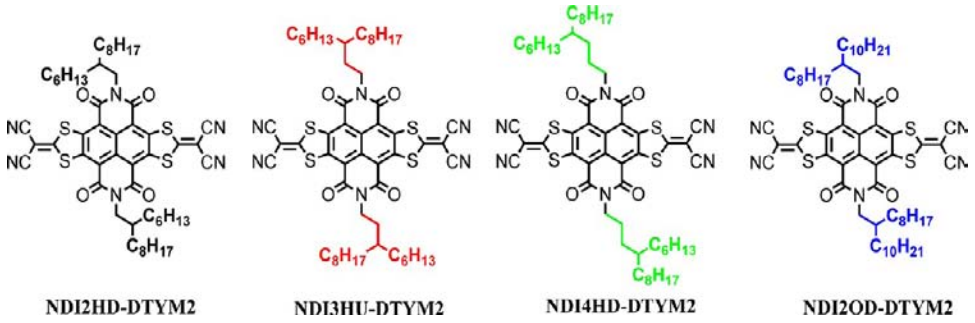

Figure 1. Molecular structures of NDI2HD-, NDI3HU-, NDI4HD-, and NDI2OD-DTYM2.

Significant improvements in semiconductor design and device engineering have resulted in much-enhanced n-channel OTFT performance and stability, enabling devices to be fabricated with a variety of solution processing techniques.[30−34,38−43] A breakthrough in n-channel polymers occurred with the development of P(NDI2OD-T2), a donor−acceptor (D−A) copolymer of 2,6-naphthalenediimide and 2,2′-bithiophene, by Watson et al. and Facchetti et al. independently.[30,39−41] Top gate OTFTs based on P(NDI2OD-T2) display electron mobilities of up to 0.85 $cm^2\ V^{-1}\ s^{-1}$.[30] Moreover, a series of small molecules based on naphthalene diimides fused with 2-(1,3-dithiol-2-ylidene)malononitrile groups (NDI-DTYM2) have also been demonstrated recently.[31−33,43] One of these derivatives, NDI2OD-DTYM2, exhibits electron mobilities as high as 0.50−1.2 $cm^2\ V^{-1}\ s^{-1}$, when appropriately processed.[32] It should be noted that the devices based on NDI2OD-DTYM2 show prominent stability which enables the construction of all solution-processed OTFTs and organic circuits under ambient atmosphere. Marder et al. recently reported solution processable bis-NDIs with conjugated bridging groups.[34] The corresponding devices exhibited field-effect mobilities of up to 1.5 $cm^2\ V^{-1}s^{-1}$, which is among the highest values for solution processed n-channel OTFTs. These results represent important steps forward for the solution-processed n-channel OTFTs.

From the point of molecular design, it has been widely accepted that an ideal air-stable solution-processed n-type materials should possess: (i) electron-deficient π-conjugated backbones that facilitate close intermolecular $\pi-\pi$ stacking and efficient electron transport; (ii) appropriate energy level (LUMO < −4.0 eV) which can ensure efficient electron injection and ambient stable electron transport; and (iii) suitable nonconjugated side chains to provide a balance between good solubility, close intermolecular stacking, and high crystallinity in the thin-film state. Compared with intensive investigations on modulation of π-conjugated backbones and energy levels, studies on alkyl chain effect have received less attention. In fact, from studies on conjugated polymers it is known that the properties of alkyl chains including alkyl chain length and density have significant influence on solution processability, molecular packing, film microstructure, and charge transport.[28,44−53] As a result, the design of appropriate side chains is becoming an important strategy to achieve high-performance solution processable semiconductors. An alkyl chain length-dependent mobility of solution processable p-type semiconductors has been reported by different groups.[44,45,50] The obvious difference in mobility is usually the result of changed film microstructure. Apart from alkyl chain length, the side-chain attachment density also has a big impact on the ordered molecular packing.[47] For example, regioregular poly(3-hexylthiophene) (P3HT) forms a lamellar structure, while poly-[5,5′-bis(3-dodecyl-2-thienyl)-2,2′-bithiophene] (PQT) and poly-(2,5-bis(3-alkylthiophene-2-yl)thieno[3,2-*b*]thiophenes) (PBTTT) exhibit more-ordered film structures. This phenomenon is mainly attributed to the low side-chain attachment density of PQT and PBTTT, which allows efficient side-chain interdigitation and three-dimensional molecular packing.[47−51] These reports clearly demonstrated that the side chain plays an important role in influencing molecular packing and determining charge transport behavior. It should be mentioned that the previous investigations are limited to the study of p-channel semiconductors; studies on the critical role of side chain on charge transport properties for n-channel organic semiconductors are thus highly desired.

Branched alkyl chains are widely used in solution processable organic semiconductors to improve their solubility and the compatibility with different solution processing techniques.[24,28,54−56] Previously it has been believed that the branched alkyl chain is an unfavorable unit in charge transport semiconductors to achieve a highly crystalline film, which is of great importance for high-performance OTFTs.[57] Inspired by the recent reports on high-performance OTFTs based on semiconductors that bear branched side chains, the application of branched alkyl chains in solution processable organic semiconductors is now attracting increasing attention.[24,30,31,43,52,54] In our previous report, we observed that the branched alkyl chain length and branching point have an influence on the electron transport property of NDI-DTYM2-based derivatives.[43] More recently, Pei et al. reported significant influence played by branching point of branched alkyl chain on the p-channel FET performance of isoindigo-based conjugated polymers.[52] These results demonstrated the critical role of branched alkyl chain on charge transport properties of solution processable organic semiconductors. In spite of these interesting progresses,[24,43,52] systematic investigation on branched alkyl chain-dependent molecular packing and device performance is still a challenging topic. It therefore makes deep insight into the relationship between the nature of the branched alkyl chain and device performance of great importance, but challenging because: (i) the introduction of long branched alkyl chain usually makes single-crystal growth difficult and limits in-depth investigation of molecular packing; (ii) a series of representative organic semiconductors with a variety of side-chain lengths and branching points should be designed to investigate the influence of branching points on OTFT mobility. As a result, in-depth study on molecular packing in thin-film state of a series of semiconductors with different branched side chains is an effective approach to achieve a deep

dx.doi.org/10.1021/ja311469y | *J. Am. Chem. Soc.* 2013, 135, 2338−2349

understanding of the important role played by branched side chains.

Herein, systematic investigation on the branched alkyl chain-dependent molecular packing and charge transport of NDI-DTYM2 derivatives (Figure 1) is reported. This study is carried out by using a combination of OTFT characterizations, atomic force microscopy (AFM), grazing incidence X-ray diffraction (GIXRD), and near-edge X-ray absorption fine structure (NEXAFS) spectroscopy. The results indicate that the properties of branched alkyl chain of NDI-DTYM2 derivatives, especially the position of branching point, critically influence the molecular packing in thin-film state. Incorporating side chains with an appropriate branching point, the molecule NDI3HU-DTYM2 displays large area, ordered molecular packing with close intermolecular stacking and exhibits an exciting electron mobility of up to 3.50 $cm^2\ V^{-1}\ s^{-1}$. The striking branched alkyl chain-dependent mobility clearly demonstrates the critical role of side-chain engineering in molecular design and contributes to a deeper understanding of the relationship between the molecular structure and the electronic properties.

2. EXPERIMENTAL SECTION

2.1. Materials Preparation. Four NDI-DTYM2 derivatives, including NDI2HD-, NDI3HU-, NDI4HD-, and NDI2OD-DTYM2, were synthesized as previously reported.[31,33,43] The fluoropolymer poly-(perfluorobutenylvinylether) (Cytop, CTL-809M) and a perfluorocarbon-containing solvent (CT-Solv.180) were purchased from Asahi Glass Corp. and used as the gate dielectric for the top-gate devices.

2.2. Device Fabrication and Measurement of OTFTs. *Fabrication of BGBC OTFTs.* An n-type heavily doped Si wafer with a SiO_2 layer of 300 nm served as the bottom-gate electrode and dielectric layer, respectively. The Au source−drain electrodes (30 nm thick) were sputtered and patterned by a lift off technique. The device channel lengths, defined as the distance between source and drain, were varied from 5 to 50 μm, and the channel width was maintained at 1.4 mm. Before deposition of the organic semiconductor, the gate dielectrics were treated with octadecyltrichlorosilane (OTS) in a vacuum oven at a temperature of 120 °C, forming an OTS self-assembled monolayer. The treated substrates were rinsed successively with hexane, ethanol, and chloroform. The organic active layer was deposited on the OTS-treated substrates by spin coating from chloroform solution (10 mg/mL). The resulting thin films were annealed at different temperatures to improve the film quality and morphology.

Fabrication of BGTC OTFTs. The thin films of NDI-DTYM2 derivatives were deposited on OTS-treated SiO_2/Si substrates by spin coating from their $CHCl_3$ solution (10 mg/mL). Thereafter, the deposited thin films were annealed at different temperatures. Gold source and drain contacts (30 nm in thickness) were deposited on the organic layer by vacuum evaporation through a shadow mask, affording a bottom-gate top contact configuration. The channel length and width were 80 and 8800 μm, respectively.

Fabrication of TGBC OTFTs. Corning 7059 glass was used as the substrate for all the top-gate devices after cleaning in an ultrasonic bath with deionized water, acetone, and isopropanol, for 5 min each. The gold source and drain electrodes were patterned by a photolithography lift-off process. Then, an organic active layer was deposited by spin coating from solution followed by an annealing treatment. Deposited by spin-coating, 500 nm of CYTOP served as the dielectric layer. Finally, 20 nm Al was deposited to serve as the gate electrodes.

Electrical Measurement of OTFTs. The OTFT measurements were carried out at room temperature using a Keithley 4200 semiconductor parameter analyzer. The mobilities were determined in the saturation regime from the equation $I_{DS} = (\mu W C_i/2L)(V_G - V_T)^2$, where I_{DS} is the drain−source current, μ is the field-effect mobility, W is the channel width, L is the channel length, C_i is the capacitance per unit area of the gate dielectric layer, and V_T is the threshold voltage.

2.3. Thin-Film Characterization. The surface morphology of the films was characterized with a Veeco Dimension 3100 atomic force microscope (Digital Instruments) operated in the tapping mode. Lab-based X-ray diffraction (XRD) experiments were carried out using a Rigaku D/max-2500 X-ray diffractometer. Synchrotron-based GIXRD measurements were carried out at the small/wide-angle X-ray scattering beamline at the Australian Synchrotron. Fourteen keV photons were used with the 2D diffraction patterns recorded on an MAR-165 CCD detector. A grazing incidence angle of 0.09° was employed that is close to the critical angle of the film, probing bulk structure. The sample-to-detector distance was calibrated using a silver behenate standard. Data acquisition times of 60 s were used with no evidence found for beam damage when comparing data taken at shorter and longer acquisition times. GIXRD data were analyzed using the software SAXS15ID version 3299. XRD data are expressed as function of the scattering vector, q, that has a magnitude of $(4\pi/\lambda)\sin\theta$, where θ is half the scattering angle and λ is the wavelength of the incident radiation.[58]

Surface-sensitive NEXAFS spectroscopy at the carbon edge were recorded at the Soft X-ray Spectroscopy Beamline at the Australian Synchrotron, Victoria, Australia.[59,60] Near perfect linearly polarized photons ($P \approx 1$) from an undulator X-ray source with a high spectral resolution of $E/\Delta E \leq 10\,000$ were focused into an ultrahigh-vacuum chamber on an ~0.4 × 1 mm sample area. X-ray absorption was measured via total-electron yield, where the signal of all photoelectrons ejected from the sample surface is measured by recording the drain current flowing from the sample. The recorded signal was normalized to the incident photon flux using the "stable monitor method", in which the sample signal is compared consecutively to a clean reference sample, and the time variations in flux measured via a gold mesh.[61] Prior to sample measurements a clean sputtered gold specimen was measured in order to determine the carbon contamination on the gold mesh, and this contamination was assumed to be stable throughout the following measurements. The normalized spectra were scaled by subtracting a background which scales according to the atomic scattering factors of the material prior to the onset of the first feature setting (A (280 eV)) and dividing by A (320 eV). X-ray energy was calibrated to the exciton peak of a highly oriented pyrolytic graphite sample. The peaks' intensities in the spectra give information about the orientation of the transition dipole moments (TDM) with respect to the plane of the substrate. The 1s (C═C) → π^* TDM is perpendicular to the conjugated ring plane of the NDI-DTYM2 molecules, and the average tilt angle of the TDM, $\langle\gamma\rangle$, can be determined from the angular dependence of the resonance intensity, I, via

$$I = 1 + (3\cos^2\theta - 1)(3\cos^2\langle\gamma\rangle - 1) \quad (1)$$

where θ is the angle of incidence of the X-ray beam.[62] The resonance intensity was determined from the peak area via peak fitting using the MatLab GUI 'Whooska' developed by Dr. Benjamin Watts.

3. RESULTS AND DISCUSSION

Four air stable n-channel solution processable NDI-DTYM2 derivatives with high electron mobility, namely NDI2HD-, NDI3HU-, NDI4HD-, and NDI2OD-DTYM2, are selected for studying structure−property relationships (Figure 1). NDI2HD-, NDI3HU-, NDI4HD-DTYM2 possess the two-, three-, and four-branched N-alkyl chains of $C_{10,6}$, $C_{11,6}$, and $C_{12,6}$, respectively, with the comparable carbon atom numbers of 16−18, to investigate the effect of branching point on the electric properties. NDI2OD-DTYM2, a well-investigated semiconductor that bears the two-branched N-alkyl chain of $C_{12,8}$ (20 carbon atoms) is also studied to make a comparison with NDI2HD-DTYM2 (16 carbon atoms) and to enable investigation on influence of side-chain length on device performance.

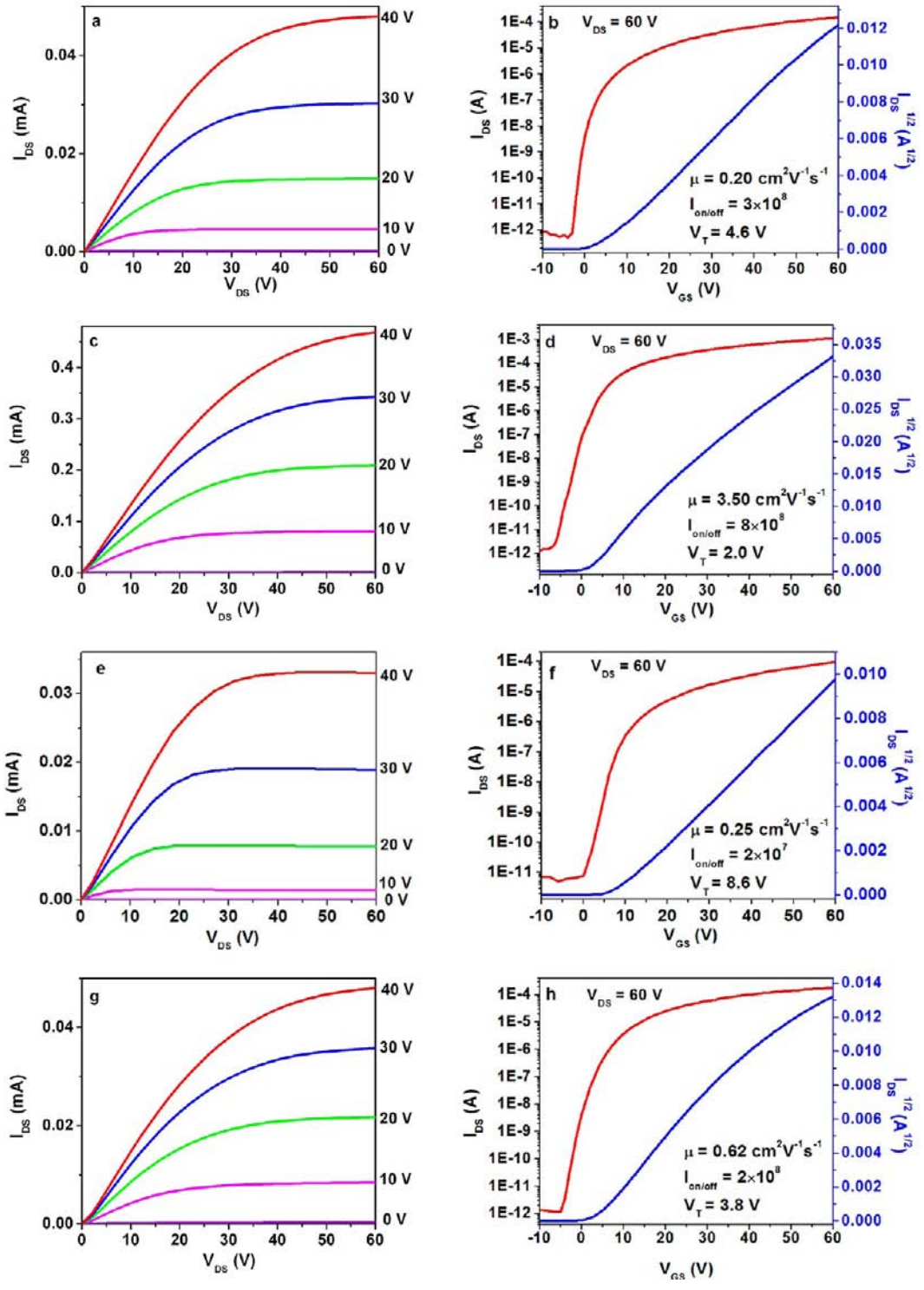

Figure 2. Output and transfer characteristics of BGBC OTFTs based on semiconductors of (a,b) NDI2HD-DTYM2; (c,d) NDI3HU-DTYM2; (e,f) NDI4HD-DTYM2; and (g,h) NDI2OD-DTYM2. Devices based on NDI2HD-, NDI3HU-, NDI4HD-, and NDI2OD-DTYM2 were fabricated by spin coating on OTS-treated Si/SiO_2 substrates annealed at 160, 160, 80, and 180 °C, respectively.

3.1. Thin-Film Transistor Characterization. OTFTs based on NDI2HD-DTYM2, NDI3HU-DTYM2, NDI4HD-DTYM2, and NDI2OD-DTYM2 were fabricated by spin-coating methods with bottom-gate bottom-contact (BGBC), bottom-gate top-contact (BGTC), and top-gate bottom-contact (TGBC) device configurations. All the devices exhibit similar characteristics in air and under N_2 atmosphere, with well-defined linear and saturation regimes (Figure 2). The bottom-gate devices show moderate hysteresis while top-gate devices exhibit very low hysteresis (Figures S1 and S2). The OTFT characteristics of the devices annealed at optimal temperatures are summarized in Table 1. The collected data clearly demonstrate the excellent device performance of optimized OTFTs with different organic active layer and different device configurations. For the OTFTs of NDI2HD-DTYM2, the BGBC showed electron mobilities of 0.15−0.34 cm^2 V^{-1} s^{-1},

dx.doi.org/10.1021/ja311469y | J. Am. Chem. Soc. 2013, 135, 2338−2349

Table 1. Optimized Device Performance of OTFTs Based on NDI-DTYM2 Derivatives with Different Device Structures[a]

device structure	semiconductor	mobility (cm^2 V^{-1} s^{-1}) av[b] (max)	threshold voltage (V) av[b] (min)	I_{on}/I_{off} av[b] (max)
BGBC	NDI2HD-DTYM2	0.20(0.34)	−0.51(0.30)	$10^5(10^7)$
	NDI3HU-DTYM2	3.03(3.50)	−2.54(0.17)	$10^7(10^8)$
	NDI4HD-DTYM2	0.24(0.25)	7.07(2.53)	10^6 (10^7)
	NDI2OD-DTYM2	0.50(0.65)	4.09(−1.96)	10^7 (10^8)
BGTC	NDI2HD-DTYM2	0.12(0.18)	12.0(5.98)	10^6 (10^7)
	NDI3HU-DTYM2	2.50(2.62)	5.79(4.63)	10^6 (10^7)
	NDI4HD-DTYM2	0.18(0.25)	8.75(5.32)	10^6 (10^7)
	NDI2OD-DTYM2	0.40(0.55)	10.4(8.78)	10^6 (10^6)
TGBC	NDI2HD-DTYM2	0.08(0.11)	10.2(8.90)	10^5 (10^6)
	NDI3HU-DTYM2	0.65(1.21)	8.85(5.21)	10^7 (10^9)
	NDI4HD-DTYM2	0.0008(0.0009)	9.50(7.80)	10^3 (10^4)
	NDI2OD-DTYM2	0.15(0.30)	8.92(4.38)	10^6 (10^8)

[a]All the films have been fabricated by spin coating and annealed at optimized temperatures. [b]The average device characteristics obtained from more than 30 devices for each materials, and the devices showed comparable performance under ambient conditions and N_2.

which are comparable to those of BGTC devices (0.10−0.18 cm^2 V^{-1} s^{-1}) and slightly higher than those of TGBC devices (0.05−0.11 cm^2 V^{-1} s^{-1}). An exciting device performance with maximum electron mobility of 3.50 cm^2 V^{-1} s^{-1}, I_{on}/I_{off} = 8 × 10^8, V_T = 2.0 V, and S = 1.39 V/dec was achieved for the BGBC devices based on NDI3HU-DTYM2. This mobility, which is a new record for the solution-processed n-channel OTFTs, approaches the performance of many excellent p- and n-channel devices based on vacuum-deposited organic semiconductors. It should be noted that the NDI3HU-DTYM2-based BGTC and TGBC devices exhibit maximum mobilities of 2.62 and 1.21 cm^2 V^{-1} s^{-1}, respectively. As for NDI4HD-DTYM2, both BGBC and BGTC devices share the same maximum electron mobility of 0.25 cm^2 V^{-1} s^{-1}, while TGBC devices display rather low mobilities of ∼0.0008 cm^2 V^{-1} s^{-1}. NDI2OD-DTYM2-based BGTC and BGBC devices exhibit maximum electron mobility of ∼0.60 cm^2 V^{-1} s^{-1}, and a lower mobility of 0.30 cm^2 V^{-1} s^{-1} was obtained for the TGBC devices. As can be concluded from the above-mentioned results, BGBC devices show superior mobilities in general relative to the performance of BGTC OTFTs, while TGBC devices exhibit the worst performances owing to the large roughness of the top surface of the organic thin film.

For each kind of device geometry, a similar trend of branched alkyl chain-dependent mobility can be clearly observed. NDI3HU-DTYM2-based BGBC, BGTC, and TGBC devices show the maximum mobility of 3.50, 2.62, and 1.21 cm^2 V^{-1} s^{-1}, respectively. These values are obviously higher than the performance of NDI2OD-DTYM2-based devices, which exhibit optimal mobilities of 0.65, 0.55, and 0.30 cm^2 V^{-1} s^{-1} for devices with BGBC, BGTC, and TGBC structures, respectively. NDI2HD- and NDI4HD-DTYM2-based OTFTs with different device geometry display a mobility ranging from 0.009 to 0.34 cm^2 V^{-1} s^{-1}. Since the difference in the side-chain length and the position of branching point constitutes the only difference for these n-channel semiconductors, it implies that the nature of the branched *N*-alkyl substituent has a profound impact on the device performance of NDI-DTYM2 derivatives.

To further investigate the side-chain effect on the device performances, we studied the dependence of the mobilities of NDI-DTYM2 derivatives-based BGBC devices on the annealing temperature. As shown in Figure 3, the mobility of

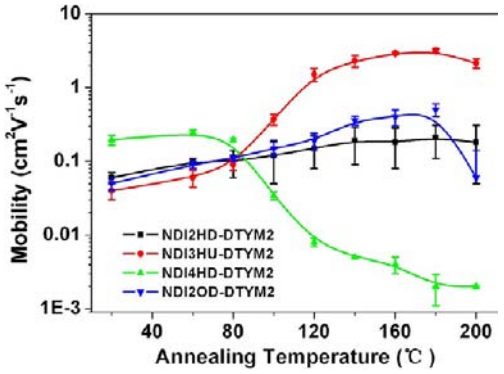

Figure 3. Device mobility of NDI-DTYM2 derivatives-based OTFTs as a function of annealing temperature.

NDI3HU-DTYM2-based devices steadily increased for annealing temperatures up to 80 °C. When the annealing temperature was >80 °C, the electron mobility of NDI3HU-DTYM2-based OTFTs improved dramatically with increasing annealing temperature. In particular the mobility increased from ∼0.03 cm^2 V^{-1} s^{-1} to well above 3.0 cm^2 V^{-1} s^{-1} after annealing at 160 °C. High mobilities of 0.5, 1.5, and 2.5 cm^2 V^{-1} s^{-1} can be achieved after annealing at 100, 120, and 140 °C, respectively, which indicates that the NDI3HU-DTYM2-based devices possess potential applications in flexible electronic applications. As for NDI2OD-DTYM2, the as-prepared devices exhibited a low mobility of 0.05 cm^2 V^{-1} s^{-1}. No obvious increase in mobility was observed after annealing at a temperature lower than 120 °C. The mobility increased dramatically to maximum values of 0.65 cm^2 V^{-1} s^{-1} after annealing at elevated temperature of up to 180 °C. NDI2HD-DTYM2-based devices display a different trend compared with OTFTs based on NDI3HU- and NDI2OD-DTYM2. When the annealing temperature increases, the mobility increased steadily from ∼0.07 to ∼0.20 cm^2 V^{-1} s^{-1}. It should be mentioned that NDI4HD-DTYM2-based devices show a different phenomenon with the as-deposited device possessing a high mobility >0.20 cm^2 V^{-1} s^{-1}, which decreases dramatically to a minimum value of 0.001 cm^2 V^{-1} s^{-1} after annealing at a temperature higher than 100 °C.

3.2. Thin-Film Microstructure. Atomic force microscopy (AFM) was utilized to investigate the surface morphologies of the fabricated thin films. Figure 4 shows the AFM images of spin-coated thin films annealed at different temperature. Although all films exhibit an ordered, terraced surface microstructure after annealing at optimal temperature, the annealing treatments lead to varied changes in morphology for different semiconductors. All as-spun films of these NDI-DTYM2 derivatives possess a similar morphology with small domain size. Obvious changes of thin-film morphology and domain size are found with increasing annealing temperature.

dx.doi.org/10.1021/ja311469y | J. Am. Chem. Soc. 2013, 135, 2338−2349

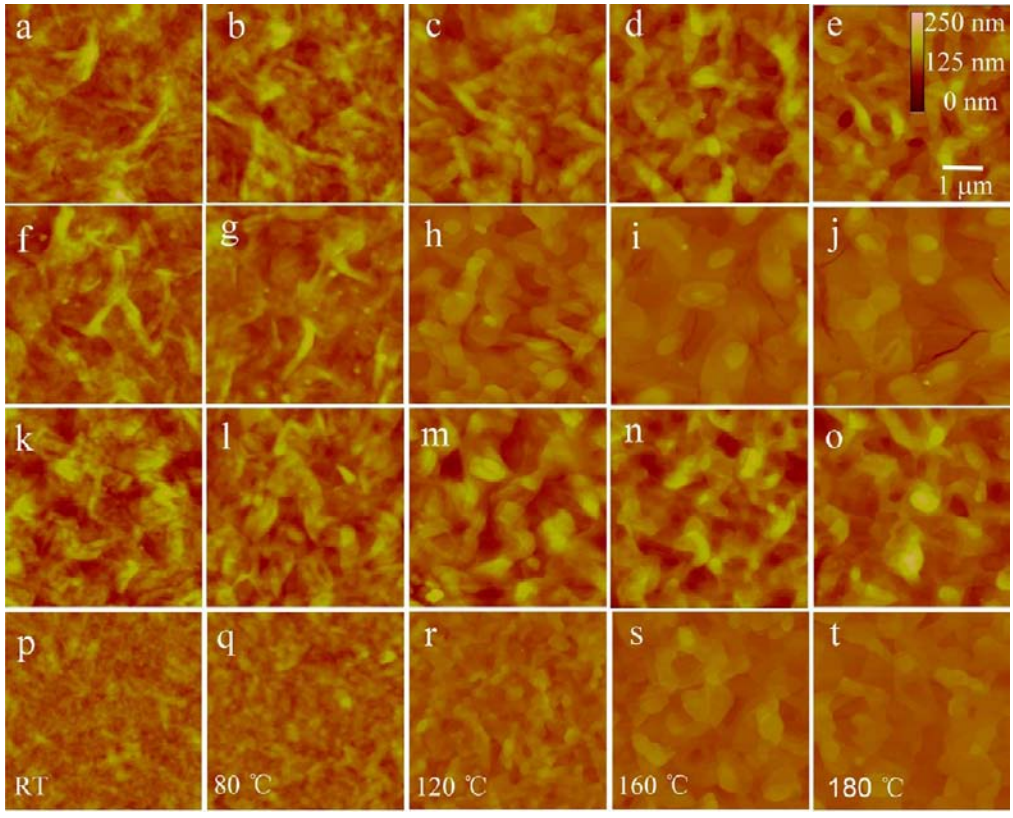

Figure 4. AFM images of thin films of (a−e) NDI2HD-DTYM2; (f−j) NDI3HU-DTYM2; (k−o) NDI4HD-DTYM2; and (p−t) NDI2OD-DTYM2 after thermal annealing at temperatures of (a,f,k,p) rt; (b,g,l,q) 80 °C; (c,h,m,r) 120 °C; (d,i,n,s) 160 °C, and (e,j,o,t) 180 °C, respectively.

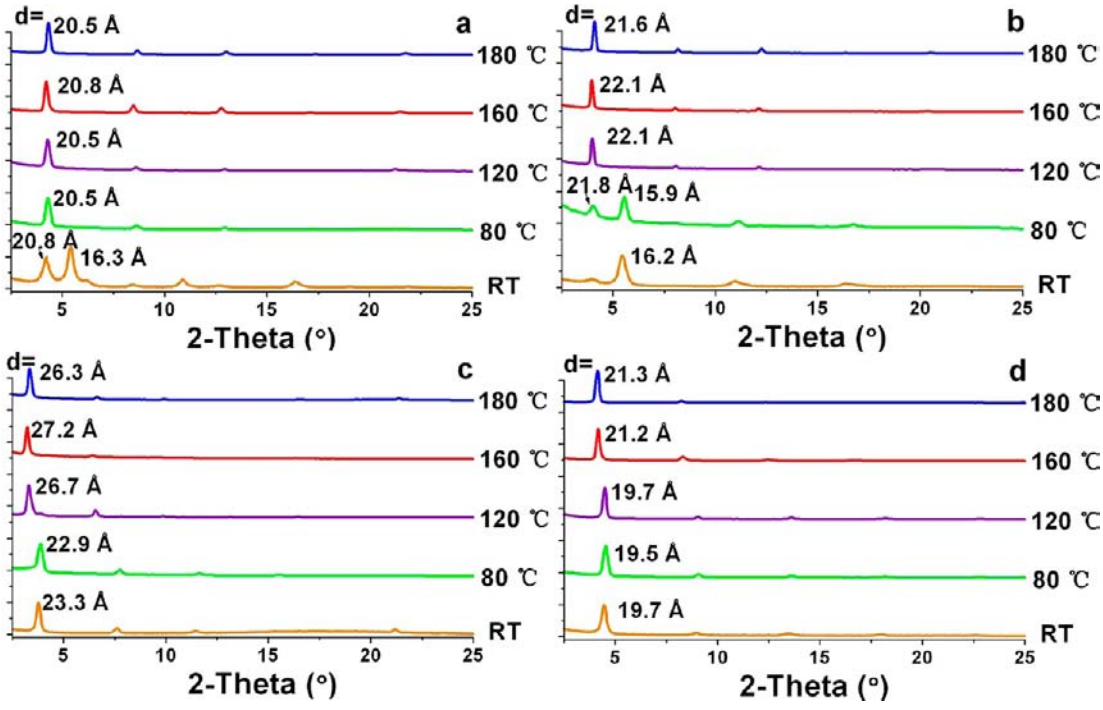

Figure 5. XRD patterns of spin-coated thin films of (a) NDI2HD-; (b) NDI3HU-; (c) NDI4HD-; and (d) NDI2OD-DTYM2 after thermal annealing at different temperatures.

NDI2HD-DTYM2 films annealed at 80−180 °C display a steadily enhanced grain size (from as-deposited 100 × 1000 to 400 × 1000 nm^2 when annealed at 180 °C). A significant film microstructure change was observed for the NDI3HU-DTYM2-based film after appropriate annealing. When the annealing temperature was >80 °C, the grain size of the NDI3HU-DTYM2-based film was enhanced dramatically from 100 × 1000 to 1000 × 3000 nm^2. In comparison with the film

dx.doi.org/10.1021/ja311469y | J. Am. Chem. Soc. 2013, 135, 2338−2349

morphology of the NDI3HU-DTYM2, the NDI4HD-DTYM2-based film appeared less crystalline (the optimal grain size value is 600 × 1000 nm^2), although obvious changes in morphology can also be observed after annealing at a temperature >80 °C. As for NDI2OD-DTYM2, the obvious morphology changes occurs at an annealing temperature >120 °C, and the optimized grain size (800 × 2500 nm^2) was slightly smaller than that of NDI3HU-DTYM2 film.

Figure 5 shows the lab-based specular XRD patterns of thin films of NDI-DTYM2 derivatives annealed at different temperatures. All the thin films exhibited sharp Bragg reflections up to third or fourth order, suggesting a high degree of crystallinity. The four NDI-DTYM2 derivatives are found to exhibit different *d*-spacing distances in thin film. More interestingly, an obvious phase transition, indicated by the change in *d*-spacing with annealing, can be observed for the thin films of these NDI-DTYM2 derivatives. The as-deposited film of NDI2HD-DTYM2 exhibits three different phases with *d*-spacing distance of 2.08, 1.63, and 1.42 nm, respectively. With annealing above 80 °C, the peak corresponding to a *d*-spacing of 2.08 nm shifts to 2.05 nm, with other peaks disappearing. In the case of NDI3HU-DTYM2, when the film is annealed at 120 °C, the reflection corresponding to a *d*-spacing at 1.62 nm disappears, and the intensity of the reflection that corresponds to a *d*-spacing of 2.21 nm is enhanced dramatically, indicating that a phase transition has occurred during thermal treatment. For NDI4HD-DTYM2, the *d*-spacing changes from about 2.30 to 2.67 nm after annealing at 120 °C. This *d*-spacing (2.67 nm) is much larger than that of the other NDI-DTYM2 derivatives (2.05−2.21 nm), suggesting the formation of a distinct molecular packing. Finally, NDI2OD-DTYM2 shows a phase transition at an annealing temperature of 160 °C. The *d*-spacing distances are 1.97 and 2.12 nm, respectively, before and after the annealing treatment.

Since single crystals of NDI-DTYM2 derivatives are difficult to grow because of the long branched side chains, thin-film grazing incidence XRD measurements were performed to study intermolecular stacking. GIXRD measurements were performed on films prepared with annealing temperatures that correspond to the optimum OTFT performance, with NDI2HD-, NDI3HU-, and NDI2OD-DTYM2 prepared with an annealing temperature of 160 °C and NDI4HD-DTYM2 prepared with an annealing temperature of 80 °C (Figure 6). GIXRD measurement was also performed on a NDI4HD-DTYM2 film annealed at 160 °C (Figure S3). As shown in Figure 6, all films possess a large number of well-defined diffraction peaks, which is remarkable for solution-processed thin films. The clarity and number of the diffraction peaks indicates a high degree of crystalline order. The diffraction patterns are characterized by a series of reflections along q_z, consistent with the peaks observed in specular lab-based diffraction (Figure 5). A number of vertical Bragg rods indicate that the films are 2D powders with the **a**−**b** unit cell vectors of all grains in the substrate plane but with random azimuthal orientation.

The unit cells of NDI2OD-, NDI2HD-, NDI3HU-, and NDI4HD-DTYM2 were obtained by fitting the measured diffraction peak positions (50, 44, 50, and 20 peaks, respectively) with a least-squares fitting method (homemade indexing software employing a modified Levenberg−Marquardt algorithm). The so-determined unit cells for NDI2OD-DTYM2: **a** = 14.25, **b** = 10.49, **c** = 22.37 Å, α = 92.4°, β = 104.0°, γ = 97.2°; NDI2HD-DTYM2: **a** = 12.46, **b** = 10.77, **c** = 20.81 Å, α = 97.6°, β = 84.9°, γ = 93.4°; NDI3HU-DTYM2: **a** = 13.60, **b** = 9.72, **c** = 21.48 Å, α = 90.7°, β = 93.8°, γ = 105.5°; and NDI4HD-DTYM2: **a** = 14.37, **b** = 9.20, **c** = 22.46 Å, α = 90.7°, β = 88.8°, γ = 112.2° are triclinic and reproduce all peak positions within an error of 0.02 Å^{-1} (within the experimental error in the area detector and scattering geometry). The unit cell volumes of 3210.7, 2752.3, 2727.8, and 2747.5 Å^3 are compatible with the assumption of a single molecule per unit cell (molecular volumes estimated from the atomic vdW radii: 3075.7, 2630.0, 2785.4, and 2650.9 Å^3), and the numerical correspondence between unit cell volumes and molecular volumes corroborates the indexing (the molecular volumes are smaller than the unit cell volumes which is a "reality check" that the indexing is physically reasonable). All peaks in the diffraction patterns of Figure 6 have been successfully indexed (see Figure S4 for details) with all films exhibiting a triclinic crystal structure with a single molecule per unit cell. Unlike the diffraction patterns of conjugated polymers, $\pi-\pi$ stacking distances cannot be directly extracted from patterns of Figure 6 as the peaks in Figure 6 correspond to the geometry of the unit cell rather than the orientation of the molecules within the unit cell. In-depth analysis based on the relative intensities of the peaks in these diffraction patterns may permit determination of the molecular configuration within the unit cell (and hence $\pi-\pi$ stacking distances). However, such analysis is time-consuming and beyond the scope of the present work. In contrast, to the well-defined patterns in Figure 6, the diffraction pattern of the NDI4HD-DTYM2 film annealed at 160 °C lacks clearly defined off-axis scattering peaks while maintaining the series of Bragg reflections along q_z (Figure S3). The absence of off-axis diffraction peaks suggests that well-defined out-of-plane stacking is maintained in the 160 °C annealed NDI4HD-DTYM2 film, while long-range in-plane crystalline order has been lost.

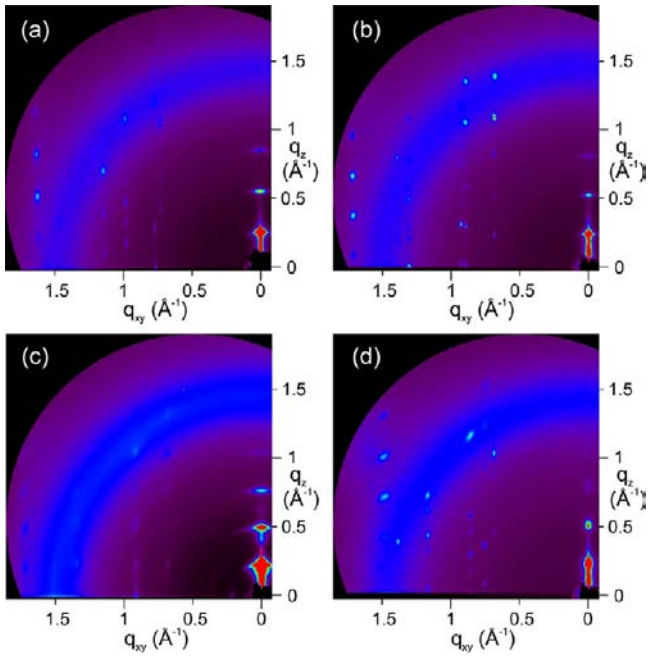

Figure 6. 2D GIXRD patterns for optimized thin film of (a) NDI2HD-; (b) NDI3HU-; (c) NDI4HD-; and (d) NDI2OD-DTYM2.

Although all OTFT-optimized films possess a similar triclinic crystal structure, some differences in the unit cell structure are noted. The four different molecules possess different in-plane

dx.doi.org/10.1021/ja311469y | J. Am. Chem. Soc. 2013, 135, 2338−2349

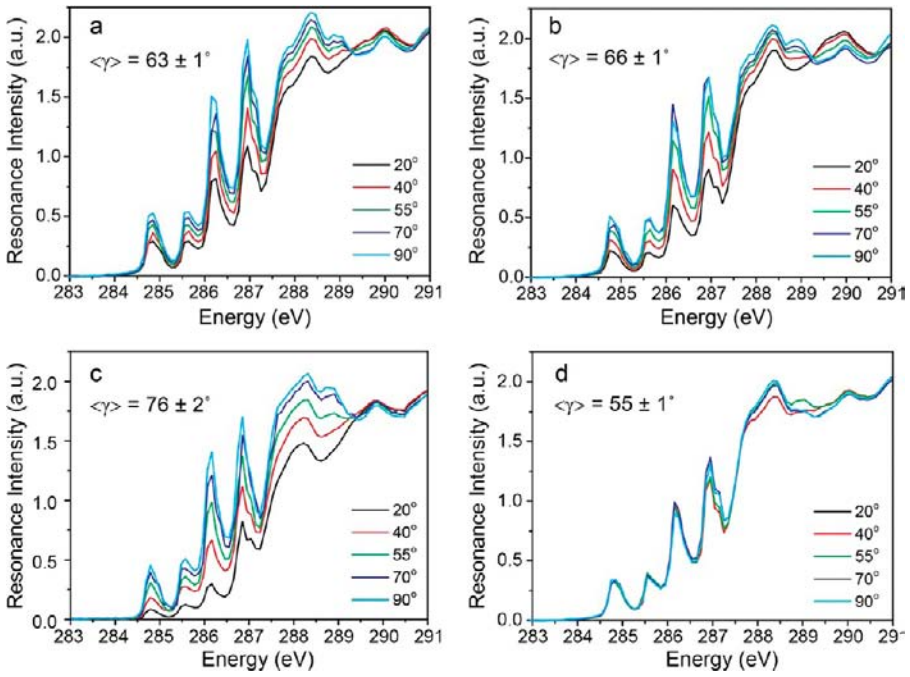

Figure 7. NEXAFS spectra of optimized thin films of (a) NDI2HD-; (b) NDI3HU-; (c) NDI4HD-; and (d) NDI2OD-DTYM2.

unit-cell areas, with the in-plane unit cell area related to how dense the aromatic units are packed in the substrate surface plane. The in-plane unit cell areas of the four molecules are found to be 133, 127, 122, and 148 Å^2 for NDI2HD-, NDI3HU-, NDI4HD-, and NDI2OD-DTYM2, respectively. NDI2OD-DTYM2 clearly has a significantly larger in-plane unit cell area than the three other compounds, consistent with a lower in-plane molecular packing density resulting from the bulkier side group of NDI2OD-DTYM2. Examining the in-plane unit cell areas of the other compounds, the lowest in-plane unit cell area is found for NDI4HU-DTYM2 which suggests that NDI4HU-DTYM2 may possess an advantage over NDI2HD- and NDI3HU-DTYM2 with regard to OTFT mobility. However, optimized NDI4HU-DTYM2 films also possess the largest angular spread of the specular peaks along q_z. The angular spread of the (00l) peaks along q_z is related to the degree of alignment of the grains to the substrate surface with larger peak spreads corresponding to greater misorientation. The grain orientation relative to the substrate is a known factor in OTFT performance of small molecules and polymer films.[63] The angular spread (FWHM) of the second specular peak at $q_z \sim 0.6$ Å^{-1} (the (020) peak) is 5.78°, 5.14°, and 4.37° for NDI4HD-, NDI2HD-, and NDI3HU-DTYM2, respectively. Thus the alignment of grains to the substrate is less faithful in optimized NDI4HD-DTYM2 films than in optimized NDI2HD- and NDI3HD-DTYM2 films. This observation is likely to be related to the fact that NDI4HD-DTYM2 films are optimized for an annealing temperature of ≤80 °C. The larger optimum annealing temperatures for NDI2HD- and NDI3HU-DTYM2 that result in improved grain size (as discerned from the AFM data) are likely to cause improved grain alignment. Indeed, the angular spread of the (020) peak in the NDI4HD-DTYM2 film annealed at 160 °C is reduced (Figure S3), however a loss of in-plane crystalline order is also brought about by annealing at 160 °C. We note that the angular spread of the (020) peak is least for NDI2OD-DTYM2 (2.89°), suggesting there is a trade-off between in-plane molecular density and grain alignment.

Angle-resolved NEXAFS spectroscopy provides information regarding the molecular orientation of the conjugated core complementary to GIXRD. The angle-dependent NEXAFS measurements were carried out on the NDI-DTYM2 films prepared in the same ways as those for GIXRD analysis. Figure 7 shows the NEXAFS spectra between 283 and 291 eV highlighting the resonant transitions found below the ionization edge. In particular the peaks between 283 and 287 eV are attributed to transitions from C-1s states to unoccupied π^* orbitals. All NDI-DTYM2 derivatives exhibit similar π^* NEXAFS structure consistent with all molecules possessing the same conjugated core. Significant differences in the degree of dichroism of the π^* peaks are found consistent with the molecules exhibiting different tilting of the planar core from the surface normal. Using eq 1 and averaging over the peaks found in the π^* manifold, the average tilt angles of the π^* TDM for NDI2HD-, NDI3HU-, NDI4HD-, and NDI2OD-DTYM2 are found to be 63°, 66°, 76°, and 55°, respectively. Thus all molecules adopt a preferential edge-on orientation to the substrate, where a tilt angle of $\gamma = 90°$ corresponding to the plane of conjugation being perfectly edge-on to the substrate and $\gamma = 0°$ being perfectly face-on to the substrate. NDI2HD-, NDI3HU-, and NDI4HD-DTYM2 all exhibit a more pronounced edge-on orientation than NDI2OD-DTYM2, which is consistent with the smaller in-plane unit cell areas measured by GIXRD. NDI4HD-DTYM2 in particular exhibits a notably high tilt angle of 76° which increases to 80° with annealing to 160 °C (Figure S5).

3.3. Discussion. For typical OTFTs, the carrier transport is mainly affected by the charge trapping in the intergrain regions and intermolecular charge transport inside the domains. Therefore, both film microstructure and intermolecular stacking play an important role in determining the device performance of OTFTs. Figure 8 summarizes the mobility of OTFTs as a function of grain size for devices based on different

dx.doi.org/10.1021/ja311469y | J. Am. Chem. Soc. 2013, 135, 2338−2349

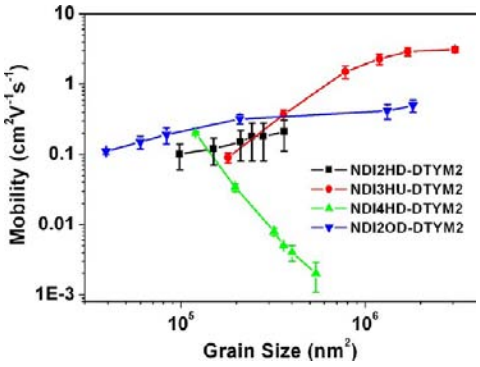

Figure 8. Extracted mobility as a function of grain size for OTFTs based on NDI-DTYM2 derivatives.

NDI-DTYM2 derivatives. The four semiconductors show different film morphology as indicated by the varied grain size ranging from 3×10^4 to 3×10^6 nm^2. Increasing grain size results in a linear increase of mobility for OTFTs based on NDI2HD- and NDI2OD-DTYM2. 4- and 60-fold enhancements in grain size lead to 2- and 5-fold improvements in mobility for NDI2HD- and NDI2OD-DTYM2-based devices, respectively. However, different phenomena are observed for NDI3HU- and NDI4HD-DTYM2-based OTFTs. In particular for NDI3HU-DTYM2 there are two linear regions in the mobility vs grain size plot. An initial increase in grain size from 2×10^5 to 8×10^5 nm^2 brings about a 15-fold improvement in carrier mobility from ∼0.1 to ∼1.5 cm^2 V^{-1} s^{-1}. A further increase in grain size from 8×10^5 to 3×10^6 nm^2 results in a steady increase in mobility from ∼1.5 to ∼3.0 cm^2 V^{-1} s^{-1}. For NDI4HD-DTYM2-based OTFTs, the electron mobility suffers from unexpected decrease from 0.2 to 0.001 cm^2 V^{-1} s^{-1} along with much enhanced grain size from 10^5 to 5×10^5 nm^2. Since the NDI-DTYM2 derivatives with different side chain show significantly different trends of grain size-dependent mobility, this indicates that the change in film morphology is not the exclusive reason for the significant variety in mobility.

Incorporating XRD results with device performance and AFM measurments provides a better understanding of grain size-dependent mobility. For NDI2HD- and NDI2OD-DTYM2, an obvious phase transition temperature occurs at 80 and 160 °C, respectively. It should be mentioned that the annealing temperature is controlled from 80 to 160 °C to avoid the influence of the solvent (when T < 80 °C) and the appearance of large cracks in the film (when T > 160 °C). Since no phase transition occurs, the steady increase of mobility for NDI2HD- and NDI2OD-DTYM2-based OTFTs is attributed to the enhanced grain size. As for NDI3HU-DTYM2-based films, the phase transition occurs at 80−120 °C with a 15-fold increase in device performance. When the annealing temperature was further increased from 120 to 160 °C, a steady increase in both grain size and extracted mobility was observed. As a result, the two different grain size-dependent linear regions for NDI3HU-DTYM2-based OTFTs with annealing temperature of 80−120 °C and 120−160 °C are ascribed to the phase transition and the enhanced grain size, respectively. In the case of NDI4HD-DTYM2, the phase transition, which occurs at 80−120 °C, appears to have a pronounced negative effect on carrier transport. The phase transition of NDI4HD-DTYM2 thin films leads to an unfavorable molecular packing and results in a 2 orders of magnitude decrease in mobility despite an increased grain size. Since the four NDI-DTYM2 derivatives possess the same conjugated core, the varied intermolecular packing, which is determined by the structure of the branched alkyl chain, is the major reason for the different mobility of the NDI-DTYM2 derivatives.

From consideration of the AFM, XRD, GIXRD, and NEXAFS measurements, the molecular packing of NDI-DTYM2 derivatives is summarized as follows (Figure 9) with key structural parameters of OTFT-optimized films were summarized in Table 2. There are three different phases in as-prepared NDI2HD-DTYM2 thin films. Annealing the film produces a single phase with much enhanced grain size, in-

Table 2. Summary of Key Parameters Determined from Structural Analysis of OTFT-Optimized Films

semiconductor	tilt angle γ	(001) d-spacing (Å)	in-plane unit cell area (Å^2)	(002) angular spread
NDI2HD-DTYM2	63°	20.8	133	5.14°
NDI3HU-DTYM2	66°	22.1	127	4.37°
NDI4HD-DTYM2	76°	23.3	122	5.78°
NDI2OD-DTYM2	55°	21.3	148	2.89°

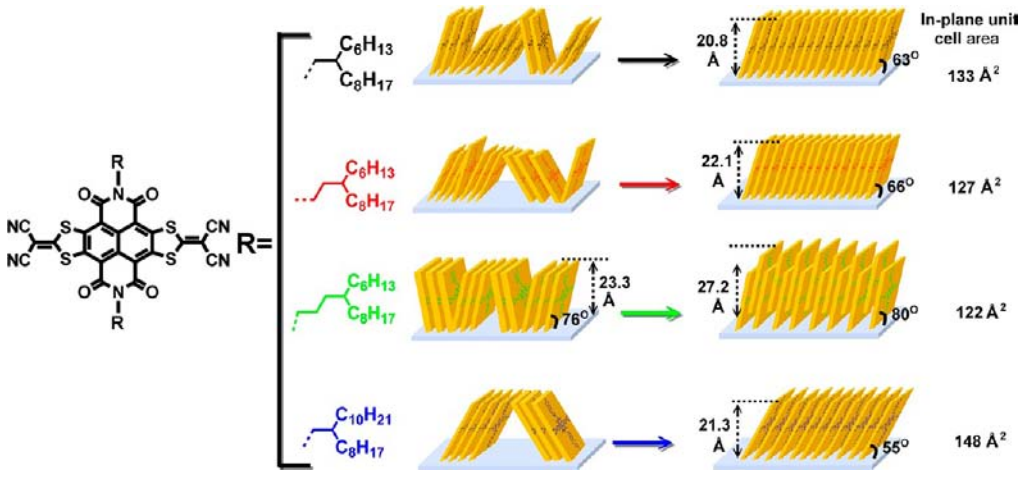

Figure 9. Schematic of molecular packing for NDI-DTYM2 derivative-based thin films before and after thermal treatments.

dx.doi.org/10.1021/ja311469y | J. Am. Chem. Soc. 2013, 135, 2338−2349

plane unit cell area of 133 Å^2, vertical *d*-spacing of 20.8 Å, and backbone tilt angle of 63°. As-spun thin films based on NDI3HU-DTYM2 show two different phases. When the NDI3HU-DTYM2 film is annealed at temperatures above 80 °C, one phase dominates with an in-plane unit cell area of 127 Å^2, *d*-spacing of 22.1 Å, and a backbone tilt angle of 66°. NDI4HD-DTYM2-based films annealed at 80 °C show a single phase with an in-plane unit cell area of 122 Å^2, *d*-spacing of 23.3 Å, and a backbone tilt angle of 80°. Annealing NDI4HD-DTYM2 at higher temperatures results in a dramatic increase in *d*-spacing from 23.3 to 27.2 Å. The much enhanced *d*-spacing value (27.2 Å) cannot be explained solely by the increased tilt angle of conjugated backbone from 76° to 80°. Therefore, the dramatic increase in *d*-spacing is probably attributed to a vertical displacement of adjacent conjugated cores as represented schematically in Figure 9. As for NDI2OD-DTYM2, a significantly larger in-plane unit cell area of 148 Å^2 is found, with a *d*-spacing of 21.3 Å and tilt angle of only 55°.

In previous reports, it has been accepted that variations in the alkyl side-chain length can have a profound impact both on intermolecular packing and orientation in thin films, which in turn can influence the electronic properties.[64] In the case of NDI2HD- and NDI2OD-DTYM2, the side-chain length increases from $C_{10,6}$ to $C_{12,8}$. This increase in side-chain length only brings about a modest increase in the (001) *d*-spacing from 2.08 to 2.13 nm. Instead, the increased chain length leads to a significant increase in the in-plane unit cell area from 133 to 148 Å^2 and a decrease in the tilt angle from 63° to 55°. Thus the change in side-chain length mainly impacts the in-plane molecular packing density. From Figure 8, NDI2HD- and NDI2OD-DTYM2 exhibit similar dependence of mobility on grain size, with the mobility of NDI2OD-DTYM2 OTFTs consistently exhibiting higher values for comparable grain sizes. The superior mobility of optimum NDI2OD-DTYM2 OTFTs may then be attributed to the significantly lower angular spread of the (002) peak of NDI2OD-DTYM2 films (2.89°) compared to NDI2HD-DTYM2 films (5.14°). Therefore, longer branched alkyl side chains promote improved molecular ordering both in terms of the assembly of large grains on OTS-modified SiO_2 substrates and lower angular misorientation of grains leading to higher charge carrier mobilities.

NDI2HD-, NDI3HU-, and NDI4HD-DTYM2 possess two-, three-, and four-branched *N*-alkyl substituents of $C_{10,6}$, $C_{11,6}$, and $C_{12,6}$, respectively. The film morphology, backbone tilt angle, and in-plane unit cell area of these three derivatives significantly change as a function of branching position, while they possess similar unit cells. Since NDI2HD-, NDI3HU-, and NDI4HD-DTYM2 have comparable side-chain length (with carbon atoms numbers of 16−18), the branching point of *N*-alkyl substituent plays a critical role in influencing intermolecular packing, which is responsible for the unprecedented differences in electron mobility ranging from 0.001 to ∼3.0 cm^2 V^{-1} s^{-1}. We suggest that the branched side-chain induced differences in molecular packing result from a competition among strong $\pi-\pi$ stacking interactions, hydrophobic interactions between the long branched alkyl chains, and the steric effect of the *N*-alkyl substitutes. A larger distance of branching point from the backbones facilitates a decrease of the steric hindrance of the branched alkyl chains and thus closer $\pi-\pi$ stacking. For the NDI-DTYM2 derivatives that have two-branched *N*-alkyl substituents of $C_{10,6}$, the steric effect limits close $\pi-\pi$ stacking. As a comparison, the three-branched *N*-alkyl substituents of $C_{11,6}$ facilitate a decrease of steric hindrance facilitating improved $\pi-\pi$ interaction. Further increase in the distance of branching point from the backbone (from three-branched *N*-alkyl substituents to four-branched ones) leads to a denser in-plane packing and almost fully edge-on molecular orientation. This efficient molecular packing contributes to the high mobility (≥0.20 cm^2 V^{-1} s^{-1}) even for the as-deposited OTFTs of NDI4HD-DTYM2, in spite of small grain size. However, the effective molecular packing of NDI4HD-DTYM2 suffers from a phase transition to another packing state after thermal treatment (>80 °C). To explain this abnormal phenomenon, we suppose that the following possible mechanism for NDI4HD-DTYM2. The changed intermolecular interaction and molecular orientation of NDI4HD-DTYM2 allows two different kinds of molecular packing, with one state favoring carrier transport and another molecular dislocation packing facilitating energy optimization. The molecular transition between these two molecular packing models occurs during the high temperature annealing (>80 °C). Although we cannot obtain two exact molecular packing states of NDI4HD-DTYM2, the XRD, AFM, GIXRD, and device performance results enable us to suppose the lateral molecular dislocation of NDI4HD-DTYM2 leads to reduced molecular overlap (even in the case of closer cofacial packing), which undermines effective charge transport in the thin film and results in the dramatic decrease in mobility. Therefore, it can be concluded that the distance of the branching point from the conjugated core affects both the intermolecular stacking and molecular arrangement significantly. Having a branched alkyl chain with the appropriate branching point is therefore of vital importance to achieving a balance of close molecular stacking, excellent crystallinity, good solubility, and prominent charge transport property in the thin-film state. Moreover, it should be mentioned that the optimal annealing temperature for NDI-DTYM2 derivatives decreased from 180 to 80 °C as the side chain changed from two-branched *N*-alkyl substituents to four-branched *N*-alkyl substituents. This phenomenon suggests that molecular engineering of side chains could provide an effective way toward modulation of the processing temperature for solution processable organic semiconductors.

4. CONCLUSION

In conclusion, we have demonstrated a systematic study on the charge transport properties of four NDI-DTYM2 derivatives having branched *N*-alkyl chain with different side-chain length and position of the branching point. A combination of detailed electrical measurements by using different OTFT geometries and thin-film characterization (AFM, XRD, GIXRD, and NEXAFS) reveals that the nature of the branched *N*-alkyl substituent has a significant influence on film morphology and molecular packing, thus affecting the charge transport properties. NDI2HD-DTYM2 (with two-branched *N*-alkyl chains of $C_{10,6}$) and NDI2OD-DTYM2 (with two-branched *N*-alkyl chains of $C_{12,8}$) share a similar molecular packing but have large differences in film morphology, indicating a moderate role of side-chain length on molecular assembly properties for NDI-DTYM2 derivatives. The improved film crystallinity of NDI2OD-DTYM2 is responsible for higher electron transport mobility (0.42−0.65 cm^2 V^{-1} s^{-1}) than that of NDI2HD-DTYM2 (0.15−0.34 cm^2 V^{-1} s^{-1}). Considering the comparable side-chain length of NDI2HD-, NDI3HU-, and NDI4HD-DTYM2 (with two-, three-, and four-branched *N*-alkyl substituents of $C_{10,6}$, $C_{11,6}$, and $C_{12,6}$, respectively), the limited

changes in the position of branching point lead to significant differences in both molecular packing and film morphology, resulting in 3 orders of magnitude of variation in electron mobility. With a three-branched alkyl chain, NDI3HU-DTYM2 films possess efficient in-plane packing and large grain sizes enabling an exciting electron mobility of up to 3.50 $cm^2 V^{-1} s^{-1}$, which is a record value for ambient stable solution-processed n-channel OTFTs. All of these results demonstrate that the molecular modulation of organic semiconductor structure via fine-tuning of branched side chains can provide an effective approach to achieve high-performance solution processable semiconductors and also aids in-depth understanding of structure−property relationships.

■ ASSOCIATED CONTENT

Ⓢ Supporting Information

Description of the material included. This material is available free of charge via the Internet at http://pubs.acs.org.

■ AUTHOR INFORMATION

Corresponding Author

dicha@iccas.ac.cn; gaoxk@mail.sioc.ac.cn; christopher.mcneill@monash.edu; zhudb@iccas.ac.cn

Author Contributions

[∇]These authors contributed equally.

Notes

The authors declare no competing financial interest.

■ ACKNOWLEDGMENTS

We acknowledge financial support from the National Natural Science Foundation (20952001, 60901050, 61171055, 20902105, and 51173200), MOST (2011CB932300), the Chinese Academy of Sciences and Beijing Municipal Education Commission (YB20098000104), Shanghai Rising-Star Program (11QA1408100), the Engineering and Physical Sciences Research Council (EP/E051804/1) the Australian Research Council (FT100100275). Part of this research was undertaken on the soft X-ray and SAXS/WAXS beamlines at the Australian Synchrotron, Victoria, Australia.

■ REFERENCES

(1) Sokolov, A. N.; Tee, B. C.-K.; Bettinger, C. J.; Tok, J. B.-H.; Bao, Z. N. *Acc. Chem. Res.* **2012**, *45*, 361−371.

(2) Di, C. A.; Zhang, F. J.; Zhu, D. B. *Adv. Mater.* **2012**, *25*, 313−330.

(3) Chang, J.-W.; Wang, C.-G.; Huang, C.-Y.; Tsai, T.-D.; Guo, T.-F.; Wen, T.-C. *Adv. Mater.* **2011**, *23*, 4077−4081.

(4) Baude, P. F.; Ender, D. A.; Haase, M. A.; Kelley, T. W.; Muyres, D. V.; Theiss, S. D. *Appl. Phys. Lett.* **2003**, *82*, 3964−3966.

(5) Chen, Z.; Lee, M. J.; Shahid Ashraf, R.; Gu, Y.; Albert-Seifried, S.; Meedom Nielsen, M.; Schroeder, B.; Anthopoulos, T. D.; Heeney, M.; McCulloch, I.; Sirringhaus, H. *Adv. Mater.* **2012**, *24*, 647−652.

(6) Dodabalapur, A. *Mater. Today* **2006**, *9*, 24−30.

(7) Zhang, H. T.; Guo, X. F.; Hui, J. S.; Hu, S. X.; Xu, W.; Zhu, D. B. *Nano Lett.* **2011**, *11*, 4939−4946.

(8) B.Mannsfeld, S. C.; Tee, B. C.-K.; Stoltenberg, R.; Chen, C. V. H.-H.; Barman, S.; O.Muir, B. V.; Sokolov, A. N.; Reese, C.; Bao, Z. *Nat. Mater.* **2010**, *9*, 859−864.

(9) Gelinck, G. H.; Huitema, H. E. A.; van Veenendaal, E.; Cantatore, E.; Schrijnemakers, L.; van der Putten, J. B. P. H.; Geuns, T. C. T.; Beenhakkers, M.; Giesbers, J. B.; Huisman, B.-H.; Meijer, E. J.; Benito, E. M.; Touwslager, F. J.; Marsman, A. W.; van Rens, B. J. E.; de Leeuw, D. M. *Nat. Mater.* **2004**, *3*, 106−110.

(10) Someya, T.; Dodabalapur, A.; Huang, J.; See, K. C.; Katz, H. E. *Adv. Mater.* **2010**, *22*, 3799−3811.

(11) Rogers, J. A.; Bao, Z.; Baldwin, K.; Dodabalapur, A.; Crone, B.; Raju, V. R.; Kuck, V.; Katz, H.; Amundson, K.; Ewing, J.; Drzaic, P. *Proc. Natl. Acad. Sci. U.S.A.* **2001**, *98*, 4835−4840.

(12) Someya, T.; Sekitani, T.; Iba, S.; Kato, Y.; Kawaguchi, H.; Sakurai, T. *Proc. Natl. Acad. Sci. U.S.A.* **2004**, *101*, 9966−9970.

(13) Sirringhaus, H. *Adv. Mater.* **2005**, *17*, 2411−2425.

(14) Usta, H.; Risko, C.; Wang, Z.; Huang, H.; Deliomeroglu, M. K.; Zhukhovitskiy, A.; Facchetti, A.; Marks, T. J. *J. Am. Chem. Soc.* **2009**, *131*, 5586−5608.

(15) Tsao, H. N.; Cho, D.; Andreasen, J. W.; Rouhanipour, A.; Breiby, D. W.; Pisula, W.; Müllen, K. *Adv. Mater.* **2009**, *21*, 209−212.

(16) Jiang, W.; Zhou, Y.; Geng, H.; Jiang, S.; Yan, S.; Hu, W.; Wang, Z.; Shuai, Z.; Pei, J. *J. Am. Chem. Soc.* **2011**, *133*, 1−3.

(17) Li, H.; Tee, B. C. K.; Cha, J. J.; Cui, Y.; Chung, J. W.; Lee, S. Y.; Bao, Z. *J. Am. Chem. Soc.* **2012**, *134*, 2760−2765.

(18) Pan, H.; Li, Y.; Wu, Y.; Liu, P.; Ong, B. S.; Zhu, S.; Xu, G. *J. Am. Chem. Soc.* **2007**, *129*, 4112−4113.

(19) Forrest, S. R. *Nature* **2004**, *428*, 911−918.

(20) Minemawari, H.; Yamada, T.; Matsui, H.; Tsutsumi, J. y.; Haas, S.; Chiba, R.; Kumai, R.; Hasegawa, T. *Nature* **2011**, *475*, 364−367.

(21) Guo, X.; Ortiz, R. P.; Zheng, Y.; Kim, M.-G.; Zhang, S.; Hu, Y.; Lu, G.; Facchetti, A.; Marks, T. J. *J. Am. Chem. Soc.* **2011**, *133*, 13685−13697.

(22) Wang, S.; Kiersnowski, A.; Pisula, W.; Müllen, K. *J. Am. Chem. Soc.* **2012**, *134*, 4015−4018.

(23) Lee, W.-Y.; Oh, J. H.; Suraru, S.-L.; Chen, W.-C.; Würthner, F.; Bao, Z. *Adv. Funct. Mater.* **2011**, *21*, 4173−4181.

(24) Chen, H.; Guo, Y.; Yu, G.; Zhao, Y.; Zhang, J.; Gao, D.; Liu, H.; Liu, Y. *Adv. Mater.* **2012**, *24*, 4618−4622.

(25) Nakayama, K.; Hirose, Y.; Soeda, J.; Yoshizumi, M.; Uemura, T.; Uno, M.; Li, W.; Kang, M. J.; Yamagishi, M.; Okada, Y.; Miyazaki, E.; Nakazawa, Y.; Nakao, A.; Takimiya, K.; Takeya, J. *Adv. Mater.* **2011**, *23*, 1626−1629.

(26) Smith, J.; Zhang, W.; Sougrat, R.; Zhao, K.; Li, R.; Cha, D.; Amassian, A.; Heeney, M.; McCulloch, I.; Anthopoulos, T. D. *Adv. Mater.* **2012**, *24*, 2441−2446.

(27) Giri, G.; Verploegen, E.; Mannsfeld, S. C. B.; Atahan-Evrenk, S.; Kim, D. H.; Lee, S. Y.; Becerril, H. A.; Aspuru-Guzik, A.; Toney, M. F.; Bao, Z. *Nature* **2011**, *480*, 504−508.

(28) Tsao, H. N.; Cho, D. M.; Park, I.; Hansen, M. R.; Mavrinskiy, A.; Yoon, D. Y.; Graf, R.; Pisula, W.; Spiess, H. W.; Müllen, K. *J. Am. Chem. Soc.* **2011**, *133*, 2605−2612.

(29) Li, J.; Zhao, Y.; Tan, H. S.; Guo, Y. L.; Di, C. A.; Yu, G.; Liu, Y. Q.; Lin, M.; Lim, S. H.; Zhou, Y.; Su, H.; Ong, B. S. *Sci. Rep.* **2012**, *2*, 754.

(30) Yan, H.; Chen, Z.; Zheng, Y.; Newman, C.; Quinn, J. R.; Dötz, F.; Kastler, M.; Facchetti, A. *Nature* **2009**, *457*, 679−686.

(31) Gao, X. K.; Di, C. A.; Hu, Y.; Yang, X.; Fan, H.; Zhang, F.; Liu, Y.; Li, H.; Zhu, D. B. *J. Am. Chem. Soc.* **2010**, *132*, 3697−3699.

(32) Zhao, Y.; Di, C. A.; Gao, X. K.; Hu, Y. B.; Guo, Y. L.; Zhang, L.; Liu, Y.; Wang, J. Z.; Hu, W. P.; Zhu, D. B. *Adv. Mater.* **2011**, *23*, 2448−2453.

(33) Hu, Y. B.; Qin, Y. K.; Gao, X. K.; Zhang, F. J.; Di, C. A.; Zhao, Z.; Li, H. Y.; Zhu, D. B. *Org. Lett.* **2012**, *14*, 292−295.

(34) Polander, L. E.; Tiwari, S. P.; Pandey, L.; Seifried, B. M.; Zhang, Q.; Barlow, S.; Risko, C.; Brédas, J.-L.; Kippelen, B.; Marder, S. R. *Chem. Mater.* **2011**, *23*, 3408−3410.

(35) Stolte, M.; Gsänger, M.; Hofmockel, R.; Suraru, S.-L.; Würthner, F. *Phys. Chem. Chem. Phys.* **2012**, *14*, 14181−14185.

(36) Wu, Q. H.; Li, R. J.; Hong, W.; Li, H.; Gao, X. K.; Zhu, D. B. *Chem. Mater.* **2011**, *23*, 3138−3140.

(37) Zhong, H.; Smith, J.; Rossbauer, S.; White, A. J. P.; Anthopoulos, T. D.; Heeney, M. *Adv. Mater.* **2012**, *24*, 3205−3211.

(38) Qiao, Y. L.; Guo, Y. L.; Yu, C. M.; Zhang, F. J.; Xu, W.; Liu, Y. Q.; Zhu, D. B. *J. Am. Chem. Soc.* **2012**, *134*, 4084−4087.

(39) Guo, X.; Watson, M. D. *Org. Lett.* **2008**, *10*, 5333−5336.

(40) Guo, X.; Kim, F. S.; Seger, M. J.; Jenekhe, S. A.; Watson, M. D. *Chem. Mater.* **2012**, *24*, 1434−1442.

(41) Chen, Z.; Zheng, Y.; Yan, H.; Facchetti, A. *J. Am. Chem. Soc.* **2009**, *131*, 8−9.
(42) Guo, X.; Ortiz, R. P.; Zheng, Y.; Hu, Y.; Noh, Y.-Y.; Baeg, K.-J.; Facchetti, A.; Marks, T. J. *J. Am. Chem. Soc.* **2011**, *13*, 1405−1418.
(43) Hu, Y. B.; Gao, X. K.; Di, C. A.; Yang, X. D.; Zhang, F.; Liu, Y. Q.; Li, H. X.; Zhu, D. B. *Chem. Mater.* **2011**, *23*, 1204−1215.
(44) Sung, A.; Ling, M. M.; Tang, M. L.; Bao, Z.; Locklin, J. *Chem. Mater.* **2007**, *19*, 2342−2351.
(45) Osaka, I.; Zhang, R.; Sauvé, G.; Smilgies, D.-M.; Kowalewski, T.; McCullough, R. D. *J. Am. Chem. Soc.* **2009**, *131*, 2521−2529.
(46) Osaka, I.; Abe, T.; Shinamura, S.; Miyazaki, E.; Takimiya, K. *J. Am. Chem. Soc.* **2010**, *132*, 5000−5001.
(47) Kline, R. J.; DeLongchamp, D. M.; Fischer, D. A.; Lin, E. K.; Richter, L. J.; Chabinyc, M. L.; Toney, M. F.; Heeney, M.; McCulloch, I. *Macromolecules* **2007**, *40*, 7960−7965.
(48) Bao, Z. N.; Lovinger, A. J. *Chem. Mater.* **1999**, *11*, 2607−2612.
(49) Ong, B. S.; Wu, Y.; Liu, P.; Gardner, S. *J. Am. Chem. Soc.* **2004**, *126*, 3378−3379.
(50) McCulloch, I.; Heeney, M.; Bailey, C.; Genevicius, K.; MacDonald, I.; Shkunov, M.; Sparrowe, D.; Tierney, S.; Wagner, R.; Zhang, W.; Chabinyc, M. L.; Kline, R. J.; McGehee, M. D.; Toney, M. F. *Nat. Mater.* **2006**, *5*, 328−333.
(51) Sirringhaus, H.; Brown, P. J.; Friend, R. H.; Nielsen, M. M.; Bechgaard, K.; Langeveld-Voss, B. M. W.; Spiering, A. J. H.; Janssen, R. A. J.; Meijer, E. W.; Herwig, P.; Leeuw, D. M. d. *Nature* **1999**, *401*, 685−688.
(52) Lei, T.; Dou, J.-H.; Pei, J. *Adv. Mater.* **2012**, *24*, 6457−6461.
(53) Mei, J.; Kim, D. H.; Ayzner, A. L.; Toney, M. F.; Bao, Z. *J. Am. Chem. Soc.* **2011**, *133*, 20130−20133.
(54) Nolde, F.; Pisula, W.; Müller, S.; Kohl, C.; Müllen, K. *Chem. Mater.* **2006**, *18*, 3715−3725.
(55) Savage, R. C.; Orgiu, E.; Mativetsky, J. M.; Pisula, W.; Schnitzler, T.; Eversloh, C. L.; Li, C.; Müllen, K.; Samorì, P. *Nanoscale* **2012**, *4*, 2387−2393.
(56) Zhan, X.; Tan, Z. A.; Domercq, B.; An, Z.; Zhang, X.; Barlow, S.; Li, Y.; Zhu, D. B.; Kippelen, B.; Marder, S. R. *J. Am. Chem. Soc.* **2007**, *129*, 7246−7247.
(57) Guo, X.; Kim, F. S.; Jenekhe, S. A.; Watson, M. D. *J. Am. Chem. Soc.* **2009**, *131*, 7206−7207.
(58) Chabinyc, M. L.; Toney, M. F.; Kline, R. J.; McCulloch, I.; Heeney, M. *J. Am. Chem. Soc.* **2007**, *129*, 3226−3237.
(59) Schuettfort, T.; Watts, B.; Thomsen, L.; Lee, M.; Sirringhaus, H.; McNeill, C. R. *ACS Nano* **2012**, *6*, 1849−1864.
(60) Cowie, B. C. C.; Tadich, A.; Thomsen, L. *AIP Conf. Proc.* **2010**, *1234*, 307−310.
(61) Watts, B.; Thomsen, L.; Dastoor, P. C. *J. Electron Spectrosc. Relat. Phenom.* **2006**, *151*, 105−120.
(62) Stöhr, J. *NEXAFS Spectroscopy*; Springer-Verlag: Heidelberg, Germany, 1992.
(63) Rivnay, J.; Mannsfeld, S. C. B.; Miller, C. E.; Salleo, A.; Toney, M. F. *Chem. Mater.* **2012**, *112*, 5488−5519.
(64) Cho, E.; Risko, C.; Kim, D.; Gysel, R.; Cates Miller, N.; Breiby, D. W.; McGehee, M. D.; Toney, M. F.; Kline, R. J.; Bredas, J.-L. *J. Am. Chem. Soc.* **2012**, *134*, 6177−6190.